LA-UR-12-22368
Approved for public release; distribution is unlimited.

Title: MARMOT simulations of Xe segregation to grain boundaries in UO2

Author(s): Andersson, Anders D.
Tonks, Michael
Casillas, Luis
Millett, Paul
Vyas, Shyam
Uberuaga, Blas P.
Nerikar, Pankaj

Intended for: Report

MARMOT simulations of Xe segregation to grain boundaries in UO_2

David A. Andersson,[1] Michael R. Tonks,[2] Luis Casillas,[1] Paul C. Millett,[2] Pankaj Nerikar,[1] Shyam Vyas,[1] and Blas P. Uberuaga[1]

[1] *Materials Science and Technology Division, Los Alamos National Laboratory, Los Alamos, NM 87545*
[2] *Fuel Modeling and Simulation, Idaho National Laboratory, P.O. Box 1625, Idaho Falls, ID 83415*

(Dated: May 31, 2012)

Diffusion of Xe and U in UO_2 is controlled by vacancy mechanisms and under irradiation the formation of mobile vacancy clusters is important. We derive continuum thermodynamic and diffusion models for Xe and U in UO_2 based on the vacancy and cluster diffusion mechanisms established from recent density functional theory (DFT) calculations. Segregation of defects to grain boundaries in UO_2 is described by combining the diffusion model with models of the interaction between Xe atoms and vacancies with grain boundaries derived from separate atomistic calculations. The diffusion and segregation models are implemented in the MOOSE/MARMOT (MBM) finite element (FEM) framework and we simulate Xe redistribution for a few simple microstructures. In this report we focus on segregation to grain boundaries. The U or vacancy diffusion model as well as the coupled diffusion of vacancies and Xe have also been implemented, but results are not included in this report.

I. INTRODUCTION

In UO_2 nuclear fuels the retention and release of fission gas atoms such as Xe are closely coupled to fuel performance. For example, the formation of fission gas bubbles induce fuel swelling, which leads to mechanical interaction with the clad thereby increasing the probability of clad breach. Fission gas bubbles also decrease the thermal conductivity of the fuel. Alternatively, fission gas can be released from the fuel to the plenum, which increases the pressure on the clad walls. In order to predict the fuel performance as function of burn-up, the redistribution of fission gas atoms must be understood. Most fission gases have low solubility in the fuel matrix, which is especially pronounced for large fission gas atoms such as Xe, and as a result there is a significant driving force for segregation of gas atoms to extended defects such as grain boundaries or dislocations and subsequently for nucleation of gas bubbles at these sinks. After segregating to grain boundaries fission gases may be released to the fuel plenum, either via fast diffusion of individual gas atoms along grain boundaries or via interlinked gas bubbles forming percolation networks.

Several empirical or semi-empirical models have been developed for fission gas release in nuclear fuels[1–6]. One of the most commonly used models in fuel performance codes was published by Massih and Forsberg[3,4,6]. This model describes release as 1) diffusion from the interior of a spherical grain to the grain boundary represented by the circumference and 2) release from the grain boundary by applying time-dependent boundary conditions to the circumference. In order to provide more detailed insight into the role of microstructure, several authors have recently applied phase field models to simulate evolution of fission gases and related properties in nuclear fuels[7–13]. Millet *et al.*[10–13] simulated void evolution and coupling between voids and fission gas atoms in metals, while Hu *et al.*[7–9] focused on similar properties in UO_2. The success of phase field models to capture the evolution of fission gases and related phenomena relies on being able to accurately represent atomistic mechanisms and to assign correct driving forces and kinetic parameters to these mechanisms. For this reason, we have derived continuum models for Xe and vacancy (Va) diffusion and grain boundary segregation in UO_2 based on mechanisms and data determined from DFT calculations and atomistic simulations[14,15].

This report is organized as follows. First we demonstrate how thermodynamic and kinetic models for Xe and vacancies in polycrystalline UO_2 fuels can be developed and parameterized using data from atomistic simulations. Next these thermodynamic and kinetic models are used to formulate transport equations for Xe and vacancy redistribution. The initial model focuses on Xe and vacancies separately. The second step where, e.g., the Xe redistribution is explicitly coupled to the vacancy dynamics is not inclued in this report. The MOOSE/MARMOT (MBM) finite element framework[17,18] is then used to solve these models for a few simple microstructures and test cases. Here we only report results from simulations of Xe segregation. This study does not aim at predicting the complete microstructure evolution, but rather investigates the rate-limiting fission gas segregation step and the detailed coupling between fission gas and vacancy diffusion.

II. THERMODYNAMIC AND KINETIC MODELS FOR XE AND VA SEGREGATION

A. Data from atomistic calculations

Nerikar *et al.* calculated grain boundary and dislocation segregation energies for Xe in UO_2 using atomistic simulations based on empirical potentials[16]. They studied three different types of grain boundaries; $\Sigma 5$ tilt, $\Sigma 5$ twist and a high angle random boundary. First they de-

termined the lowest-energy grain boundary configuration for each boundary type by applying either relative displacements of the two grains (mapping of the Γ surface) or high-temperature annealing followed by quenching to low temperature. After this they replaced one U atom with one Xe atom and calculated relative energies for Xe occupying all of the available U sites in the simulation cell. This provides data on the segregation energy as function of the distance from the boundary as well as the distribution of segregation sites at the boundary. The segregation energy is defined as the energy difference between a Xe atom occupying a bulk position far away from the grain boundary and a Xe atom positioned within the grain boundary. Note that the boundary exhibits a range of segregation energies, implying that the segregation of Xe atoms cannot be accurately represented by a single value for the segregation energy as typically applied in Langmuir-Mclean theory[19,21]. The assumption that Xe atoms reside in a single U vacancy ignores the fact that Xe atoms are believed to occupy trap sites consisting of one U and either one or two additional O vacancies in stoichiometric UO_2[15,22,23]. Nevertheless, the relative energies obtained from this simplified assumption should capture the segregation trends correctly and models could easily be adjusted to accommodate any differences emerging from coordination of Xe trap sites with O vacancies. The preferred Xe location is a function of the $UO_{2\pm x}$ stoichiometry. Unlike UO_{2-x} and stoichiometric UO_2 where Xe atoms occupy U vacancies coordinated with either one or two O vacancies, single U vacancies are the preferred Xe trap site in UO_{2+x}[15,22,23].

The segregation properties are unique for each type of grain boundary, as illustrated in Fig. 1. This conclusion refers to both the maximum sink strength, i.e. the most negative segregation energy, and the distribution of segregation sites as function of distance from the centre of the grain boundary. The random boundary is the strongest Xe sink, followed by the Σ5 tilt and Σ5 twist boundaries. Segregation of large atoms such as Xe is often described in terms of elastic interactions, i.e. the extra volume found at the grain boundary attracts the large Xe atoms by reducing the total strain of the system. This approach was, for example, applied in phase-field simulations by Hu *et al.*[7]. Close to the boundary core this description is expected to become less accurate. Nerikar *et al.* attempted to map the Xe segregation properties onto the strain obtained from atomistic simulations, but, although some correlation was found, it was difficult to quantitatively predict the segregation energy from the local strain[16]. Due to the specific atomic displacement pattern of the O sublattice at the Σ5 tilt boundary, there is an electrostatic field across the grains[24] and, since Xe occupying a single U vacancy site is a charged defect, there is an electrostatic contribution to the Xe segregation energy[16]. This gives rise to a more extended interaction range than for the other boundaries. The practical importance of this effect to nuclear fuel properties is not yet clear, since the electrostatic component could be cancelled by, e.g., associating O vacancies to Xe occupying U vacancy trap sites, by the presence of charge-compensating U^{5+} ions around the Xe trap site or by segregation of charged defects to the boundaries that exhibit an electrostatic field. The first two mechanisms make the Xe defect sites charge neutral, thus canceling any electrostatic interactions, and the latter mechanism instead removes the presence of electrostatic fields originating from grain boundaries. These details will not be further explored in this report.

Fig. 3 plots the (relative) segregation energy as function of the Xe fraction in the boundary region. This quantity was derived by independently filling available Xe trap sites, starting from the most favorable one, up to a certain site fraction and the segregation energy for this concentration is then defined as the segregation energy of the next empty Xe site. Fig. 3 illustrates that the segregation energy first increases rapidly for increasing x, after which it levels out up to $x \approx 0.9$ where the segregation energy starts rising almost exponentially. This concentration dependence must be included in order to prevent grain boundaries from becoming infinite sinks for Xe atoms. Since the segregation energy was derived from calculations of individual Xe atoms at the boundary, it neglects any explicit Xe-Xe interactions or rather, as will be explained later, they are assumed to be the same as in the bulk.

Following the approach of Nerikar *et al.* we calculated the segregation properties of U vacancies to the three grain boundary types investigated above. From Figs. 2 and 4 we conclude that vacancy segregation very closely mimics the trends already established for Xe. In order to ensure consistency we recalculated the data reported by Nerikar *et al.* using the LAMMPS code. We found good agreement with the previous study.

Andersson *et al.*[15] and Dorado *et al.*[20] calculated a large set of defect parameters in bulk $UO_{2\pm x}$ using DFT, including migration barriers and activation energies for Xe and U transport as well as binding energies for various defect clusters of critical importance for transport properties. Here this data will be used to formulate and parameterize continuum-level models for Xe and U diffusion in UO_2.

B. Thermodynamic model

1. *Xe and vacancy segregation to grain boundaries*

We would like to establish a formalism for including the detailed segregation thermodynamics outlined above in continuum-level transport models and to investigate to what extent such a model impacts the Xe and Va segregation. The most direct approach to achieve the first goal is to represent the atomistic segregation data summarized in Figs. 1, 2, 3 and 4 in an appropriate functional form. The following equation was applied for the concentration dependent Xe and Va segregation energy density,

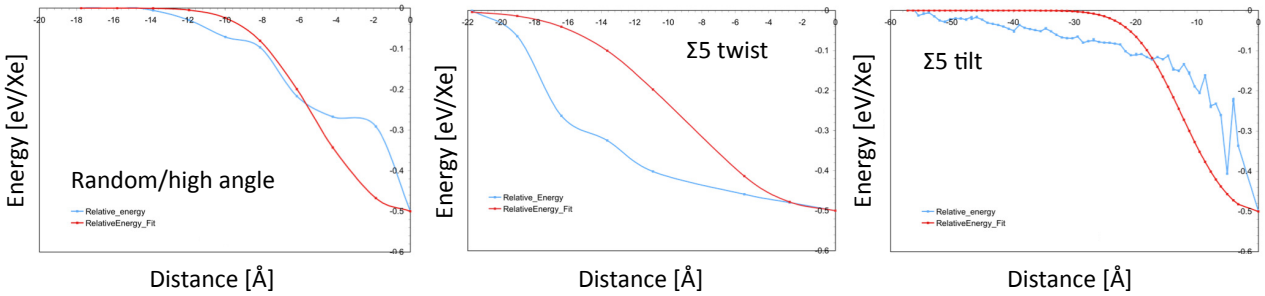

FIG. 1. The Xe segregation energy as function of the distance from the centre of the grain boundary for three different boundary types, Σ5 tilt, Σ5 twist and a high angle grain boundary classified as random (blue lines and symbols). The solid red lines illustrate Eq. 1 without the $g(y_{Xe})$ term (no concentration dependence) fitted to the lowest segregation energy as function of distance from the boundary.

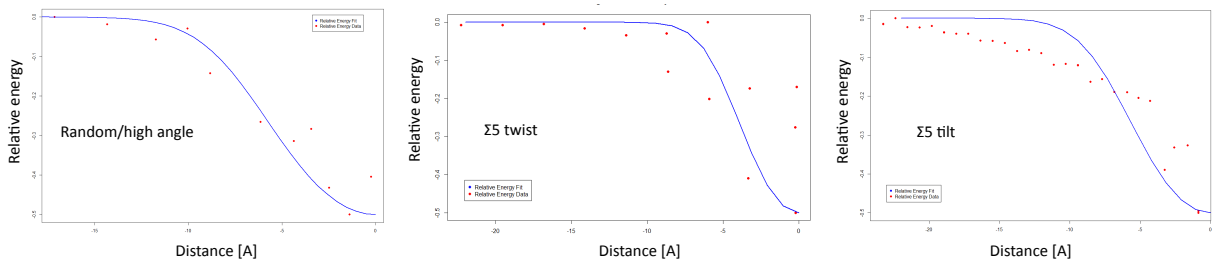

FIG. 2. The Va segregation energy as function of the distance from the centre of the grain boundary for three different boundary types, Σ5 tilt, Σ5 twist and a high angle grain boundary classified as random (red symbols). The solid blue lines illustrate Eq. 1 without the $g(y_{Va})$ term (no concentration dependence) fitted to the lowest segregation energy as function of distance from the boundary.

$E_m^{X,gb}(y_X, r)$ (where X denotes Xe or Va):

$$\frac{E_m^{X,gb}(y_X,\vec{r})}{N_A} = \\ = \sum_{i,j} \int_0^{y_X} 2\left(C_i - g_i(y'_X)\right) f_{ij}(r_{ij}) dy'_X, \qquad (1)$$

where

$$f_{ij}(r) = \frac{1}{1+\exp\left(-r_{ij}^2/k_i^2\right)} - 1 \qquad (2)$$

and

$$g_i(y_X) = m_i ln\left(100 y_X + \exp\left(\frac{-b_i}{m_i}\right)\right) + b_i \qquad (3)$$

$E_m^{X,gb}(y_X, \vec{r})$ is the total or integrated segregation energy as function of the (projected) distance from the grain boundary (r_{ij}) and the local Xe or Va concentration y_X on the cation sublattice. N_A is Avogadro's number converting the left hand side of the equation to energy per atom rather than mole. This convention will be applied throughout this work. The i index covers different types of sinks (e.g. different types of grain boundaries) and the j index covers all sinks of a specific type i (e.g. Σ5 tilt boundaries). C_i measures the dilute limit sink strength, g_i its concentration dependence and f_{ij} its spatial interaction range. The function $f_{ij}(r_{ij})$ describes the (normalized) segregation energy in the dilute limit, which is defined by the most negative segregation energy among all the grain boundary segregation sites available at a certain distance from the centre of the boundary. The most negative segregation energy is used for normalization (note that the normalization constant is in fact twice the lowest segregation energy, $2C_i$). In Eq. 2 the parameter k_i determines the slope of the Xe or Va grain boundary interaction range. For each type of grain boundary the k_i parameter was fitted to the data in Figs. 1 and 2. $g_i(y_X)$ (Eq. 3) describes the concentration dependence (y_X) of the segregation energy and the b_i and m_i parameters were fitted to the atomistic data in Figs. 3 and Figs. 4. Note that the integral in Eq. 1 measures the total segregation energy as function of the Xe or Va fraction rather than the incremental change expressed by $g_i(y_X)$ alone. Clearly this model contains a number of simplifications. For example, $g_i(y_X)$ derives from analysis of the entire grain boundary region and ignores any spatial dependence, which implies some double counting in our model. The present model for the concentration dependence is strictly speaking valid for a grain boundary that does not resolve the segregation energy as function

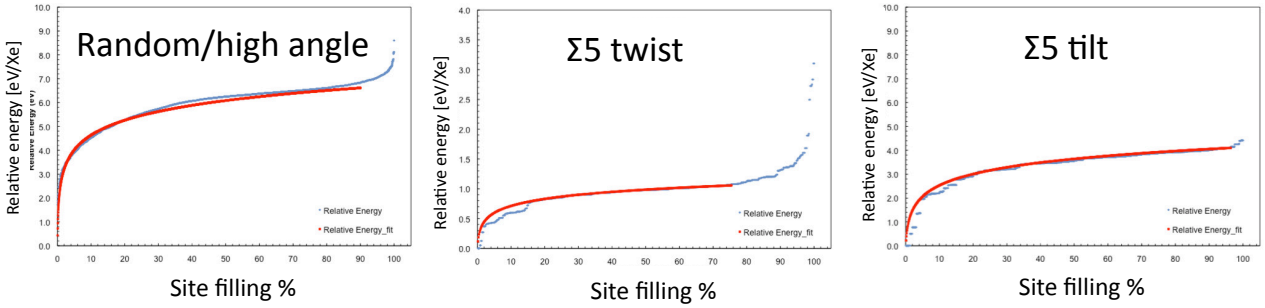

FIG. 3. The concentration dependence of the Xe segregation energy (blue lines and symbols). The solid red lines illustrate Eq. 3 fitted to the calculated data.

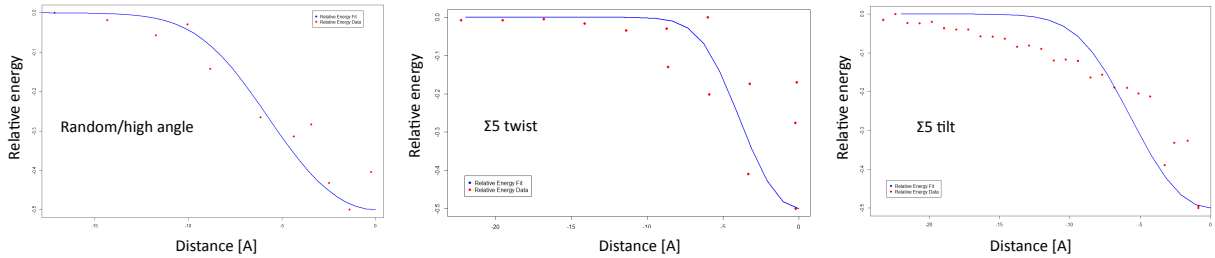

FIG. 4. The concentration dependence of the Va segregation energy (red symbols). The solid blue lines illustrate Eq. 3 fitted to the calculated data.

of distance but rather treats it as a region with a concentration dependent segregation energy given by $g_i(y_X)$ (i.e. the grain boundary is described by a step function rather than as a continuous function). Any contributions that originate from entropy differences between bulk and grain boundaries are presently ignored. The segregation energy is assumed to be independent of temperature, which ignores the statistical distribution between segregation sites expected at high tempertaure.

Table I summarizes the fitted k_i, b_i and m_i values as well as the direct calculations of C_i for each grain boundary type. The quality of the $f_{ij}(r_{ij})$ and $g_i(y_X)$ fits are in general good, which is illustrated in Figs. 1, 2, 3 and 4. Note that for some of the data in Table I the $f_{ij}(r_{ij})$ the interaction range was given a higher weight in the fitting procedure than the absolute segregation energies. We are currently investigating the balance between these two contributions. For Σ5 tilt boundaries the deviation between data points and the fitted curve originates from the presence of an electrostatic field that would require a different functional form of the f_{ij} interaction range or explicit calculation of electrostatic interactions to give optimal results. Improved representation could in principle be achieved by changing the r_{ij} exponent from 2 to 1 or some non-integer value in Eq. 2. Table I also includes the f_{ij} parameter set that describes the segregation to the Σ5 tilt boundary in the absence of electrostatic contributions. The $g_i(y_X)$ fits were performed for data points up to the concentration level indicated by the fitted red lines in Fig. 3. The upturn occurring beyond this point is ignored. This approximation has no influence on the actual simulation results since the current description still captures the saturation point for the local concentration field and, in particular, once fission gas bubble or void formation is incorporated, this process will be initiated well before reaching the local concentration limit. The models derived above refer to independent segregation of Xe and Va.

Grain boundary type	C_i (eV)	k_i (nm)	b_i	m_i
Xe				
Σ5 tilt	4.09	1.225	0.900	0.700
Σ5 tilt, no electrostatics	3.99	0.387	0.900	0.700
Σ5 twist	0.97	0.922	0.315	0.171
Random	6.42	0.469	2.562	0.900
Va				
Σ5 tilt	3.56	0.5637	-2.768	1.403
Σ5 twist	1.23	0.3890	0.111	0.317
Random	4.80345	0.5691	1.78	0.856

TABLE I. Fitted or calculated C_i, k_i, b_i and m_i parameters for Xe and Va segregation to different grain boundary types.

2. *Xe and Va bulk thermodynamics*

The thermodynamic properties of Xe and Va in bulk UO_2 are here described by the (U,Xe)O_2 and (U,Va)O_2

regular solution model. For Xe the energy density is given by (including the gradient energy terms required for capturing the dissolution kinetics):

$$\frac{G_m^{bulk}(y_{Xe},T)}{N_A} = (1-y_{Xe})\,{}^oG_U^{UO_2} + y_{Xe}\,{}^oG_{Xe}^{UO_2} + {}^0Ly_{Xe}(1-y_{Xe}) + +k_BT\left((1-y_{Xe})\ln(1-y_{Xe}) + y_{Xe}\ln(y_{Xe})\right) + +\frac{\epsilon_{Xe}}{2}\left(\nabla y_{Xe}\right)^2 + \frac{\epsilon_U}{2}\left(\nabla(1-y_{Xe})\right)^2 \quad (4)$$

y_{Xe} is the mole fraction of Xe on the U sublattice, ${}^oG_U^{UO_2}$ is the free energy of the U fluorite end-member compound, ${}^oG_{Xe}^{UO_2}$ is the free energy of the Xe fluorite end-member compound and ${}^0L$ is the regular solution parameter. The last two terms in Eq. 4 are the Xe and U gradient energy coefficients, respectively. k_B is the Boltzmann constant, which implies that all parameters in Eq. 4 are expressed in eV per atom or formula unit rather than per mole. The ${}^0L$ parameter is evaluated from atomistic calculations of the Xe-Xe binding energy (E_B), which provides ${}^0L = 6E_B \approx 10.35$ eV. This value was obtained by placing two Xe atoms in a void created by two bound Schottky defects and comparing the energy with that of Xe atoms occupying a single Schottky defect. Clearly, this is not only a measure of the Xe-Xe interaction energy, but also the first stage of Xe bubble formation. The high positive value of ${}^0L$ captures the insoluble character of Xe in UO_2 and this implies that the system is highly susceptible to spinodal-like decomposition[25]. However, this tendency is counteracted by the gradient energy terms $\frac{\epsilon_{Xe}}{2}\left(\nabla y_{Xe}\right)^2 + \frac{\epsilon_U}{2}\left(\nabla(1-y_{Xe})\right)^2$. The instability is governed by the usual relations for the critical fluctuation wavelength as function of, ${}^0L$, ϵ_U and ϵ_{Xe}. ϵ_U and ϵ_{Xe} have not been calculated yet, but were here set to 10 eV. Lower values give rise to numerical instabilities even for low concentrations of Xe. The origin of these instabilities is the high value for the ${}^0L$ interaction parameter. In some simulations we make the simplifying assumption that Xe atoms form an ideal solution on the U sublattice and, consequently, the ${}^0L$ parameter is set to zero.

The ${}^oG_{Xe}^{UO_2}$ parameter can be determined from the solution energy of Xe in UO_2, which has been calculated from DFT as function of the $UO_{2\pm x}$ stoichometry[15]. The Xe reference state is defined as the gas phase at 298 K and 100000 Pa. The ${}^oG_U^{UO_2}$ reference is arbitrarily set to 0 eV. The Xe trap sites in UO_2 involves more complex defects than the U vacancy site assumed in Eq. 4. At the UO_2 composition the Xe atom is likely associated with additional O vacancies, however for simplicity this contribution is not explicitly contained in the present formulation. Instead ${}^oG_{Xe}^{UO_2}$ is adjusted to represent the active defect configuration for the composition of interest. The ${}^oG_{Xe}^{UO_2}$ parameter does not enter the present diffusion simulations, since the simulations only consider one phase but this term would be required for capturing the relative stability of Xe atoms in fission gas bubbles and in solution. Table II collects the bulk thermodynamic model parameters in Eq. 4. The regular solution model captures the interactions between Xe atoms, but the entropy contribution is not modified. Obviously, this is a simplification and extensions from this model have been demonstrated using various degrees of complexity within alloy theory. However, for the present simulations the neglect of entropy corrections is viewed as a minor simplification.

The thermodynamic properties of vacancies in UO_2 are described using the same model as for Xe (Eq. 4). Based on results from DFT calculations the ${}^oG_{Va}^{UO_2}$ and ${}^0Ly_{Va}$ parameters were calculated to be 3.39 eV and -1.0 eV, respectively (see Table II).

Note that in Eq. 4, as well as throughout this work, the O sublattice is not explicitly treated, which is motivated by the fact that the dynamics on the anion sublattice is several orders of magnitude faster than the corresponding dynamics on the cation (U) sublattice. This implies that we assume quasi-equilibrium conditions to prevail such that the O sublattice is in equilibrium with the instantaneous species distribution on the cation sublattice. Similar simplifications are applied to any species on interstitial sublattices.

U-Xe model		
	Low irr.	High irr.
${}^oG_U^{UO_2}$ (eV)	0	0
${}^oG_{Xe}^{UO_2}$ (eV)	5.24	5.24
${}^0L_{XeU}$ (eV)	10.35	10.35
ΔQ_0 (eV)	3.94	3.18
ΔH_{Xe} (eV)	5.29	5.29
D_0 (nm/s^2)	$5\cdot10^{12} - 5\cdot10^{14}$	N/A
U-Va model	Low irr.	High irr.
${}^oG_U^{UO_2}$ (eV)	0	0
${}^oG_{Va}^{UO_2}$ (eV)	3.39	3.39
${}^0L_{UVa}$ (eV)	-1.0	-1.0
ΔQ_0 (eV)	4.22	2.92
ΔH_U (eV)	4.75	4.75
ΔH_{U2} (eV)	2.61	2.61
D_0^U (nm/s^2)	$2\cdot10^{11}$	$2\cdot10^{11}$
D_0^{U2} (nm/s^2)	$2\cdot10^{11}$	$2\cdot10^{11}$

TABLE II. Bulk thermodynamic and kinetic parameters for the Xe-U and U-Xe-Va models, respectively, under thermal equilibrium conditions (Low irr.) and under irradiation (High irr.). The two separate estimates for each parameter were obtained from two different DFT data sets (see Ref. 15 for details).

3. Xe and Va bulk and grain boundary thermodynamics

The complete thermodynamic models for Xe and Va in UO_2 are obtained as the sum of Eqs. 1 and 4:

$$\frac{G_m^{Total}\left(y_X, T, \vec{r}\right)}{N_A} = \frac{G_m^{bulk}\left(y_X, T\right)}{N_A} + \\ + \sum_{i,j} \int_0^{y_X} 2\left(C_i - g_i(y'_X)\right) f_{ij}(r_{ij}) dy'_X. \quad (5)$$

Here the superscript X denotes either Xe or Va. Note that the distances r_{ij} are defined as the orthogonal projection from the position $\vec{r}$ to the grain boundaries. If the grain boundary network is represented by connected line segments the sum in Eq. 5 can be evaluated for each point in the simulation domain. The projection is only included in the summation if it is within the spatial bounds of the line segment. Regions where the sum over different i and/or j overlap, such as grain boundary triple junctions, require special attention. As an alternative to inter-connected line segments the grain structure can be represented by a phase-field model in which each grain i is described by an order parameter ϕ_i. $\phi_i = 1$ within this grain and zero in all other grains. It varies continuously from one to zero over the boundary. At a point on a boundary, several order parameters have values between zero and one. In the phase field description the sum in Eq. 5 is over the number of possible pairings between order parameters with values greater than zero (to be revisited in order to improve descriptions of grain boundary triple junctions). The index i denotes the properties of the grain boundary type defined by the current order parameter pair. The spatial interaction is defined as $f_i = \Phi_i - 1$, where $\Phi_i = \phi_j^2 + \phi_k^2$. ϕ_j and ϕ_k are the current order parameter pair. One benefit of reformulating the original model applying line segments into a phase field model is to facilitate coupled simulations of gas bubble evolution and grain growth. Furthermore, compatibility with existing phase field models for simulating nuclear fuel properties is ensured[7,8,10–13]. All simulations presented here apply the phase-field model.

C. Kinetic model

1. Xe and Va mobilities

In order to simulate Xe transport the (atomic) mobility of Xe (M_{Xe}) must be determined. Since Xe moves via a vacancy mechanism the relevant quantity governing Xe diffusion is the (atomic) mobility multiplied by the vacancy fraction, $M_{Xe}y_{Va}$ (according to reaction rate theory). The Xe vacancy mechanism is somewhat unique in the sense that the vacancy is bound to the Xe trap site, which affects both the mobility and flux equations. Exceptions to vacancy-mediated diffusion may occur for transients in high irradiation fields, as discussed in Ref. 14 for Xe interstitials migrating via the O sublattice. $M_{Xe}y_{Va}$ is related to the measured or calculated Xe activation energy (ΔQ) via the Arrhenius relation $M_{Xe}y_{Va} = \frac{D_0}{k_B T}\exp\left(-\frac{\Delta Q}{k_B T}\right)$. The exact value of ΔQ depends on the details of the Xe diffusion mechanism, which is a function of the $UO_{2\pm x}$ stoichiometry[15]. In this study we assume stoichiometric UO_2, for which $\Delta Q_0 = E_F^{V_U} - E_B + E_m^{C,V_U} = 3.9$ eV from experiments[26]. Here $E_F^{V_U}$ is the U vacancy formation energy, E_m^{C,V_U} is the migration barrier and E_B is the binding energy of U vacancies to the Xe trap sites. DFT calculations of the individual defect parameters provide a very similar estimate for the activation energy (3.94 eV), which will be used in the present simulations. This estimate applied the point defect model derived in Ref. 20 to calculate the effective vacancy formation energy in UO_2, which explains the slightly lower activation energy compared the prediction in Ref. 15. The former value is believed to better correspond to the experimental conditions. The derivation of ΔQ_0 assumes that diffusion occurs via thermal vacancies, however under irradiation the vacancy concentration is expected to increase. For high non-thermal vacancy concentrations $E_F^{V_U}$ should be set to zero, which gives us $\Delta Q_0 = -E_B + E_m^{C,V_U} = -0.81 + 5.29 = 4.48$ eV. However, for a constant vacancy production rate the vacancy concentration will be proportional to $\exp\frac{1.3}{k_B T}$. This factor derives from the fact the the annealing of vacancies scales as one over the square root of the vacancy mobility. Under irradiation the relevant vacancy migration energy is 2.61 eV. Based on this relation $\Delta Q_0 = 3.18$ eV. Unfortunately, the pre-exponential factor is not known and it is difficult to estimate for this case.

Finally, the Xe mobility is calculated as the product of a pre-exponential factor D_0 and the exponential of the activation energy (Arrhenius model).

$$M_{Xe}y_{Va} = \frac{D_0}{k_B T}\exp\left(-\frac{\Delta Q}{k_B T}\right) \quad (6)$$

The pre-exponential factor is taken to be $D_0 = 5 \cdot 10^{13}$ nm^2/s,[26] which was obtained from experiments on Xe diffusion.

The mobility of vacancies or equivalently U atoms is expressed as:

$$M_U = \frac{D_0}{k_B T}\exp\left(-\frac{\Delta H_U}{k_B T}\right) \quad (7)$$

As for Xe the relevant quantify for U diffusion is $M_U y_{Va}$ (according to reaction rate theory). Under local thermal equilibrium $M_U y_{Va}$ is given by the activation energy according to $M_U y_{Va} = \frac{D_0}{k_B T}\exp\left(-\frac{\Delta Q}{k_B T}\right)$. For stoichiometric UO_2 we have calculated the activation energy to be 4.22 eV, which is very close the experimental value of 4.4 eV. The actual migration barrier is $\Delta H_U = 4.75$ eV and the activation energy is obtained by calculating the effective vacancy formation energy according to the model presented in Ref. 20. However, it is not really meaningful

to calculate vacancy segregation under thermal equilibrium and consequently all our simulations apply a model where the factor y_{Va} is explicitly treated and the mobility given by Eq. 7. DFT calculations have highlighted the importance of U vacancy clustering for explaining experimental measurements of U vacancy migration barriers in damaged materials[15]. In order to model effects of U vacancy clustering a second mobility must also be introduced for U, M_{U_2}.

$$M_{U_2} = \frac{D_0}{k_B T} \exp\left(-\frac{\Delta H_{U_2}}{k_B T}\right) \tag{8}$$

ΔH_{U_2} was calculated to be 2.61 eV and represents the mobility of two bound U vacancies. The relevant quantity is $M_{U_2} y_{Va_2}$, where y_{Va_2} denotes the site fraction of di-vacancy clusters.

The pre-exponential factor was taken as $D_0 = 2 \cdot 10^{11}$ nm^2/s[26] for U vacancies. This value was derived from vacancy diffusion in irradiated samples and for this reason it should not include any contributions from defect formation reactions or equilibria.

D. Transport equations

1. Xe-U model

As explained in Ref. 15, Xe diffuses via a vacancy mediated mechanism where the vacancy is bound to the Xe trap site and this implies that diffusion effectively occurs via a U exchange mechanism. For the Xe-U model the Onsager linear law applied to the lattice flux of Xe via the vacancy mediated exchange mechanism yields:

$$J_{Xe} = -L_{Xe} \nabla \left(\mu_{Xe} - \mu_U\right). \tag{9}$$

Here $\mu_{Xe} - \mu_U$ is the chemical potential difference between Xe and U and its spatial gradient, $\nabla\left(\mu_{Xe} - \mu_U\right)$, represents the driving force for diffusion of Xe. For a regular vacancy diffusion mechanism the driving force would be $\nabla\left(\mu_{Xe} - \mu_{Va}\right)$. The magnitude of the resulting flux, J_{Xe}, is controlled by the linear flux parameter, L_{Xe}. According to reaction rate theory the flux parameter is of the form $L_{Xe} = M_{Xe} c_{Xe} y_{Va} = \frac{M_{Xe} y_{Xe} y_{Va}}{V_m}$, where M_{Xe} is the Xe mobility for vacancy assisted diffusion, y_{Xe} and y_{Va} are the site fractions of Xe and Va on the U sublattice, respectively, and $c_{Xe} = \frac{y_{Xe}}{V_m}$ is the concentration of Xe. The combined factor $M_{Xe} y_{Va}$ was defined in Eq. 6. $\nabla(\mu_{Xe} - \mu_U)$ can be calculated from the free energy density in Eq. 5 according to non-equilibrium thermodynamics, which is equivalent to applying the Cahn-Hilliard equation.

$$\mu_{Xe} - \mu_U = \frac{\delta}{\delta y_{Xe}} \left(\int_\Omega G_m^{Total} d\Omega\right)_{y_{Xe}+y_U} = \\ = \left(\frac{\partial G_m^{Total}}{\partial y_{Xe}}\right)_{y_{Xe}+y_U} - \nabla \cdot \left(\frac{\partial G_m^{Total}}{\partial \nabla y_{Xe}}\right)_{y_{Xe}+y_U}. \tag{10}$$

The subscript $y_{Xe} + y_U$ indicates that $y_U = 1 - y_{Xe}$ is treated as the dependent variable.

The time evolution of the Xe concentration field in the lattice fixed frame of reference is governed by the usual conservation law:

$$\frac{\partial\left(y_{Xe}/V_m\right)}{\partial t} = -\nabla \cdot J_{Xe}. \tag{11}$$

y_{Xe}/V_m is equal to the concentration (c_{Xe}) of Xe. In order to mimic fission events a homogeneous source term $\eta(t)$ may be added to Eq. 11, similar to previous models by Hu *et al*[7] and Millet *et al.*[10–12]. The molar volume is assumed to be constant.

2. U-Va model

U diffuses via a vacancy mechanism, for which the flux is:

$$J_U = -L_U \nabla\left(\mu_U - \mu_{Va}\right) = \\ = -\frac{M_U y_{Va} y_U}{V_m} \nabla\left(\mu_U - \mu_{Va}\right) \tag{12}$$

L_U is a kinetic parameter given by $M_U y_{Va} y_U$. Andersson *et al.* also investigated the influence of U and O vacancy clustering on the activation energy for U (or equivalently U vacancy) diffusion. They concluded that when there are a significant number of non-thermal vacancies due to irradiation, clustering spontaneously occurs and this lowers the U (vacancy) migration barrier from 4.75 to 2.61 eV. The above equation (Eq. 12) does not account for the clustering of U vacancies. However, if we assume local equilibrium in each grid point this effect can be obtained from the following reaction.

$$Va_U + Va_U \rightleftharpoons (Va_U Va_U) \tag{13}$$

The corresponding reaction energy is $\Delta E = 0.17$ eV. In a scenario where the U vacancies bind with oxygen vacancies created via irradiation this interaction becomes attractive, but, as we will see below, even for slightly positive binding energies there are enough clusters to dominate diffusion under irradiation. The fraction of bound vacancies, $y_{VaVa} = y_{Va_2}$, is calculated by applying the law of mass action to reaction 13.

$$J_U = -L_U \nabla\left(\mu_U - \mu_{Va}\right) = \\ = -\frac{M_U\left(y_{Va} - y'_{Xe} - y_{Va_2}\right) y_U}{V_m} \nabla\left(\mu_U - \mu_{Va}\right) \\ -\frac{M_{U_2} y_{Va_2} y_U}{V_m} \nabla\left(\mu_U - \mu_{Va}\right) \tag{14}$$

The local clustering reaction determining y_{Va_2} are presently not solved in a coupled way.

The chemical potential difference that provide the driving forces for diffusion, $\mu_U - \mu_{Va}$, is derived according to

non-equilibrium thermodynamics, which is equivalent to applying the Cahn-Hilliard equation.

$$(\mu_U - \mu_{Va}) = -(\mu_{Va} - \mu_U) = \\ = \frac{\delta}{\delta y_U}\left(\int_\Omega G_m^{Total} d\Omega\right)_{y_U + y_{Va}} = \\ = \left(\frac{\partial G_m^{Total}}{\partial y_U}\right)_{y_U + y_{Va}} - \nabla \cdot \left(\frac{\partial G_m^{Total}}{\partial \nabla y_U}\right)_{y_U + y_{Va}}. \quad (15)$$

The subscript $y_U + y_{Va}$ indicates that $y_{Va} = 1 - y_U - y_{Xe}$ is treated as the dependent variable and the subscript $y_{Xe} + y_U$ that $y_U = 1 - y_{Xe} - y_{Va}$ is used. The final transport model is obtained by applying the continuity equation to the U flux equation.

$$\frac{\partial (y_U / V_m)}{\partial t} = -\nabla \cdot J_U. \quad (16)$$

The molar volume is assumed to be constant.

E. Numerical simulations

The transport equations derived in Sec. II C are solved using the MOOSE/MARMOT (MBM) framework developed at Idaho National Laboratory[17,18]. In order to avoid numerical instabilities occurring for low species concentrations due to the logarithm terms in the free energy formulation we introduced 1) a taylor expansion of the logarithm and associated derivatives for $y < 10^{-9}$ and 2) a source term for $y < 10^{-10}$. The latter term is needed to prevent concentrations from reaching negative values when the Taylor expansion is used for $y < 10^{-9}$, which mimics generation of vacancies when the concentration drops below the equilibrium value. The one-dimensional simulations of segregation to grain boundaries were performed using a uniform mesh, since adaption caused instabilities. This issue is currently under invesitigation. The two dimensional simulations applied non-uniform adaptive meshing, which improved efficiency as well as accuracy close to boundaries. All simulations used variable time steps.

III. RESULTS AND DISCUSSION

1. *Simulations of Xe redistribution in UO_2*

First Xe redistribution was simulated for bicrystal microstructures with either Σ5 twist, Σ5 tilt or random grain boundaries. We first run simulations with ${}^0L$ parameter set to zero in order to avoid instabilities related to spinodel-like decomposition. Results for initial homogeneous Xe concentration of 0.001 are illustrated in Fig. 5. All simulations were performed at 1500 K and apply periodic boundary conditions. The size of the simulation domain was 500 × 10 nm, which mimics the one dimensional character of this problem. Figs. a), b) and c) represent steady-state solutions, though note that nucleation of fission gas bubbles is not included in the present model. Figs. d), e) and f) illustrate the distribution after about 3600 s. The highest Xe concentration is reached for Σ5 tilt and the random boundary, followed by the Σ5 twist boundary. The latter has significantly lower maximum concentration. The Σ5 tilt boundary thus seems to be a stronger or at least as strong sink as the random boundary, despite having a lower segregation energy than the random boundary (see Table I). For short times the random boundary attracts more Xe, but due to the slower (with respect to y_{Xe}) increase in the concentration term, $g_i(y_{Xe})$, the Σ5 tilt boundary eventually attracts the most Xe. The longer interaction range of this boundary also plays a role for the segregation dynamics. Due to the low initial concentration none of the boundaries reached their saturation level. In order to illustrate this we also performed the same simulation with $y_{Xe} = 0.01$ as the initial concentration.

For the $y_{Xe} = 0.01$ initial concentration each boundary reached higher maximum concentration (see Fig. 6). The bulk concentration is also higher than for the $y_{Xe} = 0.001$ case. For the higher initial concentration it is clear that the Σ5 tilt boundary is a stronger sink than the random boundary. Σ5 twist boundary still reaches much lower Xe concentration than the other cases. Differences in the effective grain boundary width, measured by the region exhibiting increased concentration of Xe can also be seen in the figures. In addition to the increase in Xe concentration at the grain boundaries we also identify a minimum in-between the boundary and the bulk for the transient parts of the simulations (see Figs. 5d, e, f and 6 d, e, f). This feature indicates that, as expected, the grain boundaries attract Xe atoms faster than the supply from the interior of the grains and the segregation process is thus controlled by long-range diffusion through the bulk. In the initial steps Xe is quickly accumulated from the near-boundary region, while the growth rates decease significantly once the depleted region reaches close to zero concentration levels and becomes dominated by long-range diffusion.

The simulations above were performed with the ${}^0L$ parameter set to zero in order to avoid instabilities related to spinodel-like decomposition. We also performed simulations for the DFT calculated value of ${}^0L = 10.35$ eV and these results are illustrated in Fig. 7. For $y_{Xe} = 0.001$ the figures illustrate the concentration after about 3600 s. For $y_{Xe} = 0.01$ the system wants to separate into Xe rich regions, an indication of early stages of spinodal decomposition. Since this happens almost instantaneously the simulation time is very short. The decomposition occurs close to the boundary where the segregation leads to changes in the Xe concentration that cause the instabilities. This is clearly evidenced by the sinusoidal wave across the boundary. The driving force for spinodal decomposition is much smaller at $y_{Xe} = 0.001$ and there is no sinusoidal wave across the boundary. Compared to the ${}^0L = 0$ case the concen-

tration at the boundary increases more rapidly, which is a consequence of the higher driving force caused by the non-zero ${}^0L$ term. The unstable character of the PDEs is also evidenced by the short time steps that are required for convergence. Once the concentration at the boundary reaches significant levels it is clear that the system strives to decompose into Xe rich and poor regions. From this we conclude that once the Xe concentration reach critical level the system will spontaneously decompose into Xe rich and poor regions that may act as nucleation sites for the formation of Xe bubbles. With the current simulation settings this is unlikely to occur in bulk UO_2 if the the concentration level is less than 0.001, however this limit should easily be reached at defects such as grain boundaries where bubbles are thus expected to nucleate first. Comparing the ${}^0L = 10.35$ eV and ${}^0L = 0$ eV simulations, the former case gives rise to more Xe segregation and segregation also occurs faster. For the $y_{Xe} = 0.001$ initial concentration the difference in Xe concentration after 3600 s ranges from 50 to 100%. The reason for the decomposition reaction not occurring at the actual grain boundary in the simulations applying ${}^0L = 10.35$ eV could be threefold; 1) the concentration is not yet high enough due to the limited amount of Xe in the small simulation cell, 2) the critical fluctuation wavelength for the present choice of gradient energy coefficient is longer than the size of the grain boundary or 3) the current segregation model favors uniform concentration along the boundary.

Fig. 8a) (ideal solution) and b) (regular solution) illustrate Xe redistribution for an idealized polycrystalline sample containing $\Sigma 5$ twist, $\Sigma 5$ tilt and random grain boundaries. The size of the simulation domain is 250×216.5 nm. All simulations were performed at 1300 K, homogeneous initial distribution of $y_{Xe} = 0.001$ was prescribed and periodic boundary conditions were imposed. The difference between the grain boundary types follow the same trend as for the bicrystal simulations. The maximum concentration reached in these simulations are somewhat smaller than for the bi-crystal simulations, which may be related numerical accuracy. This issue is currently being investigated. Also, the segregation time scales are somewhat shorter for the polycrystal, even though the final concentrations are similar. The reason for this could be that the region of low Xe concentration just outside the grain boundaries acts as a more efficient barrier for the bicrystal than for the hexagonal grain geometry (further analysis under way). The difference in Xe concentration at the various boundaries would likely influence the rate of gas bubble nucleation and growth.

IV. CONCLUSIONS

This report summarizes the derivation of thermodynamic and kinetic models describing Xe and U vacancy redistribution in polycrystalline UO_2 at the meso-scale with specific focus on Xe interaction with sinks such as various types of grain boundaries and the importance of defect clustering under irradiation. We have emphasized the connection to atomistic simulations by demonstrating that unknown parameters can be obtained from existing atomistic studies.

The Xe redistribution model is implemented in the MOOSE/MARMOT (MBM) finite element framework and solved for various microstructures, in particular grain boundary distributions and different initial conditions. The simulations capture the segregation of Xe to grain boundaries and the unique characteristics of different boundary types clearly emerge from these simulations. For short time scales random boundaries are the strongest sinks for Xe, but when the local Xe concentration increases the $\Sigma 5$ tilt overtakes the random boundary as the strongest sink. The $\Sigma 5$ twist boundary attracts significantly less Xe than the other two cases. The use of a realistic values for the interaction between Xe atoms leads to spinodal-like decomposition for concentrations above $y_{Xe} = 0.001$.

[1] A. H. Booth, A method of calculating gas diffusion from UO_2 fuel and its application to the X-2-f test, Technical Report AECL 496 CRDC-721, Atomic Energy of Canada Limited (1957).

[2] M. V. Speight, Nucl. Sci. Eng. **37**, 180 (1969).

[3] K. Forsberg and A. R. Massih, J. Nucl. Mater. **135**, 140 (1985).

[4] K. Forsberg and A. R. Massih, J. Nucl. Mater. **127**, 141 (1985).

[5] K. Forsberg and A. R. Massih, Modelling Simul. Mater. Sci. Eng. **15**, 335 (2007).

[6] D. D. Lanning, C. E. Beyer and C. L. Painter, "FRAPCON-3: Modifications to Fuel Rod Material Properties and Performance Models for High-Burnup Application" (1997).

[7] S.-Y. Hu, C. H. Henager Jr, H. L. Heinisch, M. Stan, M. I. Baskes and S. M. Valone, J. Nucl. Mater. **392**, 292 (2009).

[8] S.-Y. Hu, C. H. Jr. Henager, Acta Mater. **58**, 3230 (2010).

[9] Y. L. Li, S. Y. Hu, X. Sun, F. Gao, C. H. Henager Jr and M. Khaleel, J. Nucl. Mater. **407**, 119 (2010).

[10] P. C. Millett, D. Wolf and T. Desai, J. Appl. Phys. **104**, 033512 (2008) .

[11] P. C. Millett, A. El-Azab, S. Rokkam and M. Tonks and D. Wolf, Comput. Mater. Sci. **50**, 949 (2011).

[12] P. C. Millett, A. El-Azab and D. Wolf, Comput. Mater. Sci. **50**, 960 (2011).

[13] P. C. Millett and M. Tonks, Curr. Opin. Solid State Mater. Sci. **15**, 125 (2011).

[14] X.-Y. Liu, B. P. Uberuaga, D. A. Andersson, C. R. Stanek, and K. E. Sickafus, Appl. Phys. Lett. **98**, 151902 (2011).

[15] D. A. Andersson, B. P. Uberuaga, P. V. Nerikar, C. Unal and C. R. Stanek, Phys. Rev. B **84**, 054105 (2011).

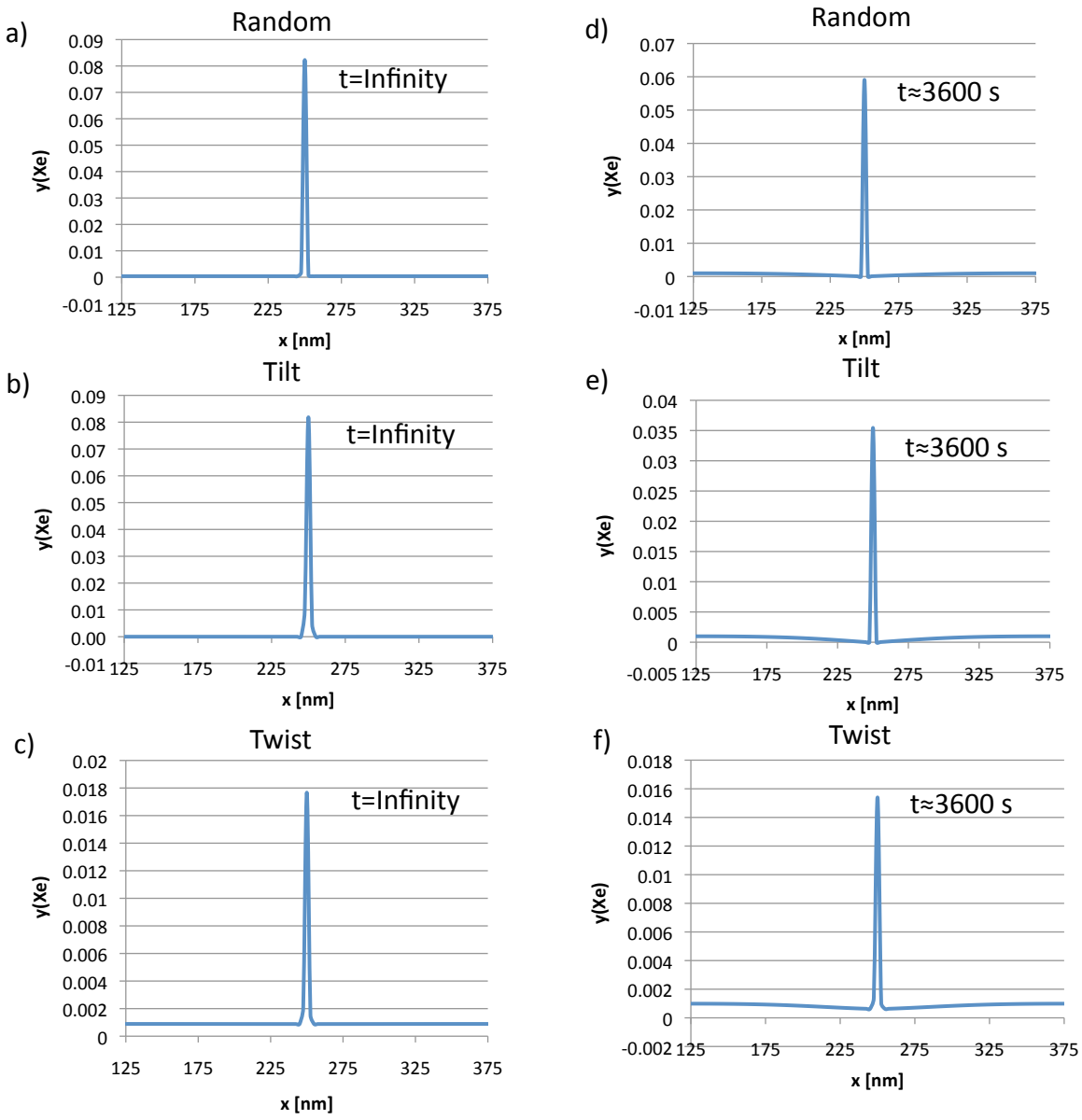

FIG. 5. Xe distribution in a bicrystal composed of a) random, b) Σ5 tilt and c) Σ5 twist grain boundaries. The domain size is 500 × 10 nm, but only visualized in the x direction. For all cases the initial state was a homogeneous distribution of Xe ($y_{Xe} = 0.001$). U-Xe is treated as an ideal solution ($^0L = 0$ eV).

[16] P.V. Nerikar, D. C. Parfitt, L. A. Casillas Trujillo, D. A. Andersson, C. Unal, S. B. Sinnott, R. W. Grimes, B. P. Uberuaga and C. R. Stanek, submitted to Phys. Rev. B.

[17] D. Gaston, G. Hansen, S. Kadioglu, D. Knoll, C. Newman, H. Park, C. Permann and W. Taitano, J. Phys.: Conf. Ser. **180**, 012012 (2009).

[18] M. Tonks, D. Gaston, C. Permann, P. Millett, G. Hansen and D. Wolf, Nucl. Eng. Design **83**, 2877 (2010).

[19] D. McLean, Grain Boundaries in Metals (London: Oxford University Press), 1957.

[20] B. Dorado, D. A. Andersson, P. Garcia, B. P. Uberuaga, G. Martin, M. Freyss, M. Bertolus, and C. R. Stanek, submitted.

[21] M. P. Seah, J. Phys. F: Metal Phys., **10**, 1043 (1980).

[22] R. G. J. Ball and R. W. Grimes, Chem. Soc., Faraday Trans. **86**, 1257 (1990).

[23] P. V. Nerikar, X.-Y. Liu, B. P. Uberuaga, C. R. Stanek, S. R. Phillpot and S. B. Sinnott, J. Phys.-Condens. Mat. **21**, 435602 (2009).

[24] P. Nerikar, C. R. Stanek, S. R. Phillpot, S. B. Sinnott and B. P. Uberuaga, Phys. Rev. B **81**, 064111 (2010).

[25] J. W Cahn, Acta Mater. **9**, 795 (1961).

[26] Hj. Matzke, J. Chem. Soc., Faraday Trans. 2 **83**, 1121 (1987).

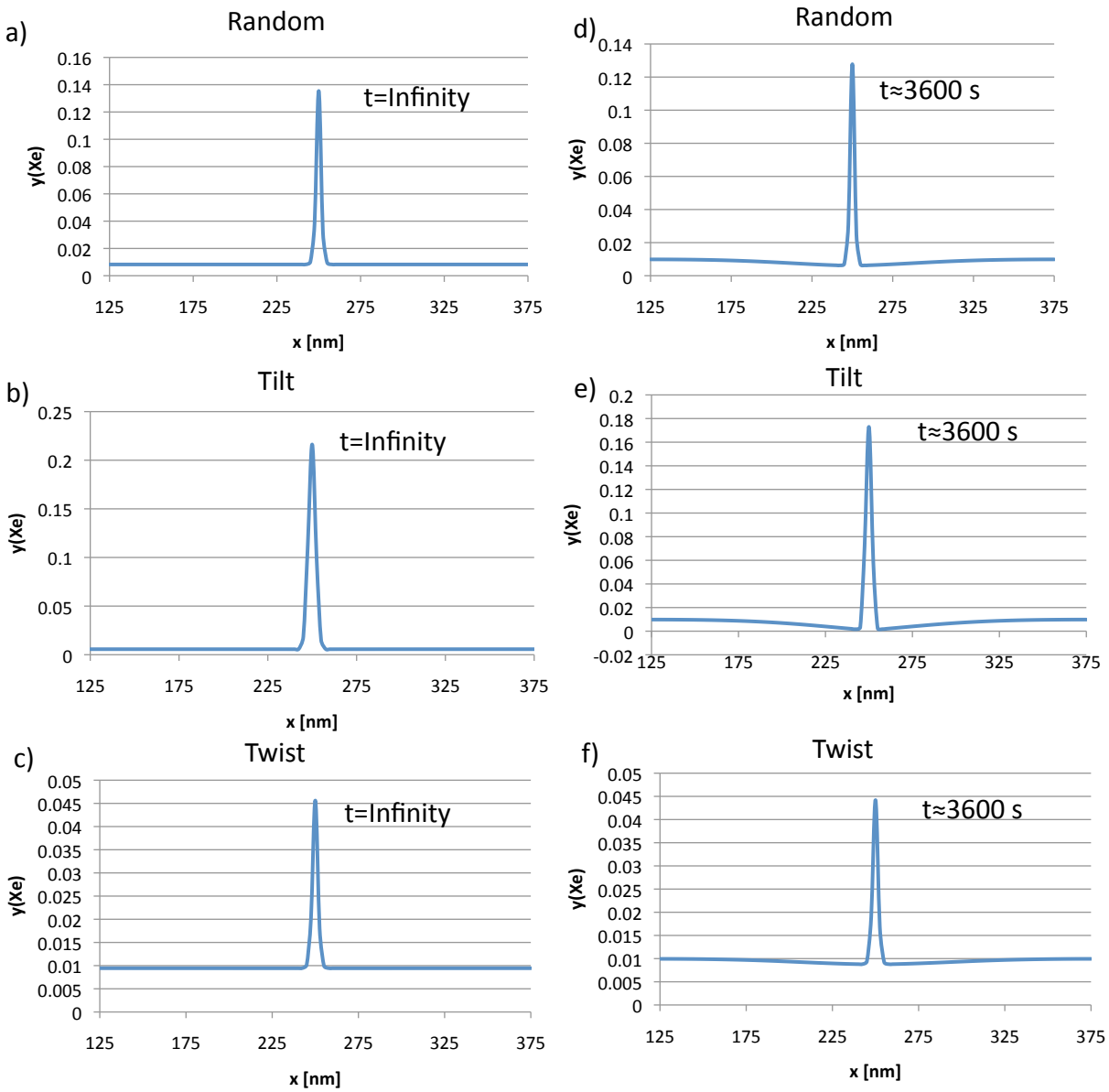

FIG. 6. Xe distribution in a bicrystal composed of a) random, b) Σ5 tilt and c) Σ5 twist grain boundaries. The domain size is 500 × 10 nm, but only visualized in the x direction. For all cases the initial state was a homogeneous distribution of Xe ($y_{Xe} = 0.01$). U-Xe is treated as an ideal solution ($^0L = 0$ eV).

[27] D. R. Olander, Fundamental Aspects of Nuclear Reactor Elements, NTIS, ERDA, 1975.

[28] N. Moelans, B. Blanpain, P. Wollants, CALPHAD **32**, 268 (2008) .

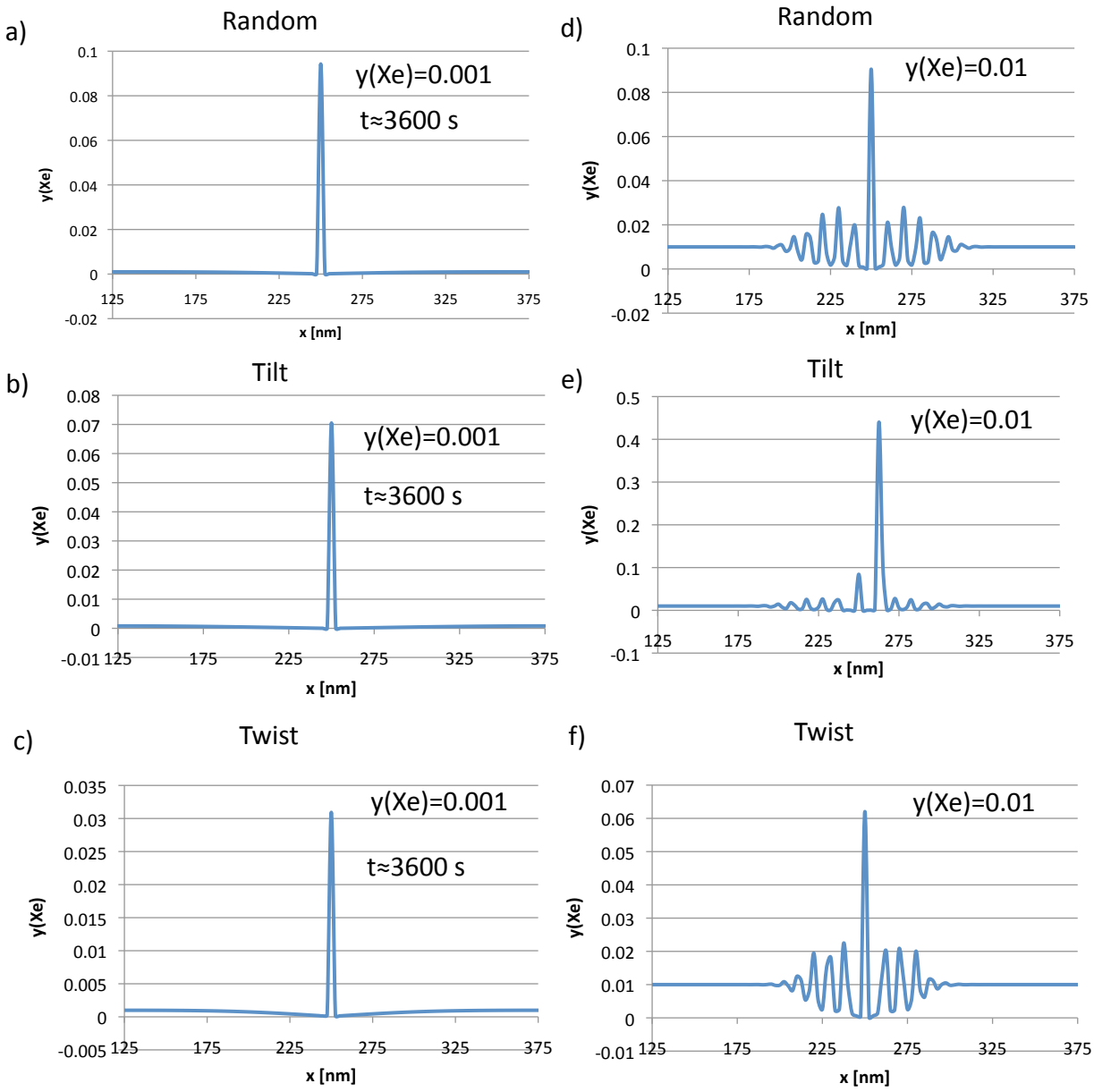

FIG. 7. Xe distribution in a bicrystal composed of a) random, b) Σ5 tilt and c) Σ5 twist grain boundary. The domain size is 500 × 10 nm, but only visualized in the x direction. For all cases the initial state was a homogeneous distribution of Xe ($y_{Xe} = 0.001$). U-Xe is treated as an regular solution ($^0L = 10.35$ eV).

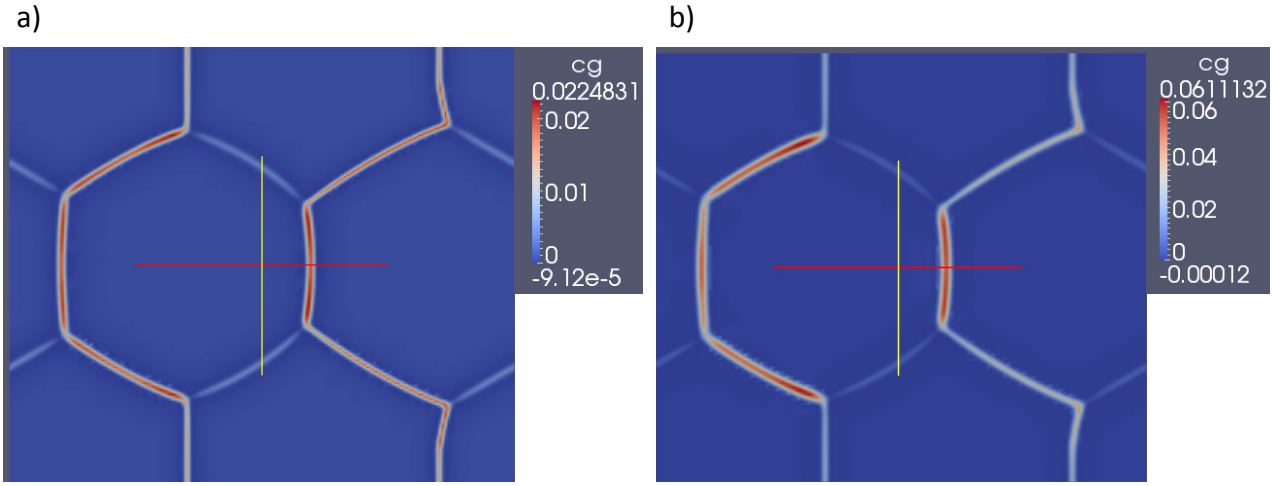

FIG. 8. a) Xe distribution for microstructure composed of random, Σ5 tilt and Σ5 twist grain boundaries. The Xe-Xe interaction parameter was set to 0 (${}^0L$=0 eV). b) Xe distribution for microstructure composed of random, Σ5 tilt and Σ5 twist grain boundaries. The Xe-Xe interaction parameter was set to 0 (${}^0L$=10.35 eV). For both cases the domain size is 250 × 216.5 nm and the initial state was a homogeneous distribution of Xe ($y_{Xe} = 0.001$).